

A Combined Theoretical and Experimental Study of Oxygen Vacancies in Co_3O_4 for Liquid-Phase Oxidation Catalysis

Amir Omranpour,^{1,2,*} Lea Kämmerer,³ Catalina Leiva-Leroy,⁴ Anna Rabe,³ Takuma Sato,⁵ Soma Salamon,³ Joachim Landers,³ Benedikt Eggert,³ Eugen Weschke,⁶ Jean Pascal Fandré,⁷ Ashwani Kumar,⁷ Harun Tüysüz,^{7,8} Martin Muhler,⁴ Heiko Wende,³ and Jörg Behler^{1,2}

¹*Lehrstuhl für Theoretische Chemie II, Ruhr-Universität Bochum, 44780 Bochum, Germany*

²*Research Center Chemical Sciences and Sustainability, Research Alliance Ruhr, 44780 Bochum, Germany*

³*Faculty of Physics and Center for Nanointegration Duisburg-Essen (CENIDE), University of Duisburg-Essen, 47057 Duisburg, Germany*

⁴*Laboratory of Industrial Chemistry, Ruhr-Universität Bochum, 44780 Bochum, Germany*

⁵*Max Planck Institute for Chemical Energy Conversion, 45470 Mülheim an der Ruhr, Germany*

⁶*Helmholtz-Zentrum Berlin für Materialien und Energie (HZB), 12489 Berlin, Germany*

⁷*Heterogeneous Catalysis and Sustainable Energy, Max-Planck-Institut für Kohlenforschung, Kaiser-Wilhelm-Platz 1, 45470 Mülheim an der Ruhr, Germany*

⁸*Catalysis and Energy Materials Group, IMDEA Materials Institute, Calle Eric Kandel 2, 28906, Getafe, Madrid, Spain*

(Dated: November 25, 2025)

In the present work, we investigate oxygen vacancies (V_O) in Co_3O_4 , both in the bulk phase and under liquid-phase ethylene glycol oxidation, by combining theoretical and experimental techniques. Density functional theory calculations for bulk Co_3O_4 show that introducing an oxygen vacancy reduces two adjacent Co^{3+} ions to Co^{2+} and narrows the band gap. The newly formed Co^{2+} ions adopt high-spin configurations in distorted octahedral sites and remain stable in this state in *ab initio* molecular dynamics simulations at 300 K. Computed O and Co K-edge X-ray absorption spectra for ideal and vacancy-containing Co_3O_4 show excellent agreement with the experimental data and serve as references to analyze the liquid-phase ethylene glycol oxidation. The comparison with experimental O K-edge spectra of fresh and post-reaction catalysts shows that fresh samples resemble the vacancy-containing reference, whereas post-reaction spectra shift toward the ideal reference. These results suggest that under liquid-phase ethylene glycol oxidation conditions, Co_3O_4 becomes more oxidized rather than reduced, by refilling preexisting oxygen vacancies. This is further supported by the observation that higher O_2 pressures increase the conversion and that the catalyst remains stable and active over several cycles.

I. INTRODUCTION

Cobalt oxide is a mixed-valence transition metal oxide that has gained considerable attention due to its distinctive chemical, physical, and electronic characteristics. Among its various forms, the cobalt spinel phase Co_3O_4 has been extensively investigated owing to its outstanding performance in oxidation catalysis, particularly in selective hydrocarbon oxidation^{1–3}. The coexistence of Co^{2+} and Co^{3+} ions in Co_3O_4 gives rise to versatile redox activity, high catalytic performance, tunable electronic structure, and intriguing magnetic behavior^{4–12}. These properties make Co_3O_4 an attractive material for a broad range of technological and industrial applications, including oxidation catalysis of alcohols¹³, water oxidation^{14,15}, methane combustion¹⁶, and CO oxidation¹⁷, as well as in lithium-ion batteries and gas sensors¹⁸.

Structurally, Co_3O_4 adopts a cubic $Fd\bar{3}m$ spinel structure in which cobalt exists in two oxidation states, Co^{2+} and Co^{3+} . The Co^{2+} ions occupy the tetrahedral interstitial sites, while Co^{3+} ions reside in the octahedral

sites within the face-centered cubic (FCC) lattice formed by oxygen anions (Figure 1). The crystal field splits the five-fold degenerate d orbitals of cobalt into two distinct energy levels. As a result, high-spin Co^{2+} exhibits three unpaired d electrons, corresponding to an experimental magnetic moment of $3.26 \mu_B$ ¹⁹, whereas Co^{3+} adopts a low-spin configuration with a nearly quenched magnetic moment (Figure 1). At ambient temperature, Co_3O_4 behaves as a paramagnetic semiconductor and becomes antiferromagnetic below 40 K¹⁹, mainly due to weak exchange interactions between neighboring Co^{2+} ions. Co_3O_4 is an intrinsic p -type semiconductor; its charge transport between 220–400 K occurs predominantly via small-polaron hopping of holes, while in the 170–220 K range it proceeds through variable-range hopping^{20,21}. The estimated experimental band gap of Co_3O_4 is approximately 1.6 eV^{22,23}.

In heterogeneous catalysis, Co_3O_4 is recognized for its effectiveness in the oxygen evolution reaction and, more recently, in alcohol oxidation. Increasing attention has been directed toward performing such oxidation reactions in the liquid phase^{13,24}, often in alkaline solution, which enables milder reaction conditions and improved selectivity²⁵. Nevertheless, the precise influence of the

* amir.omranpour@rub.de

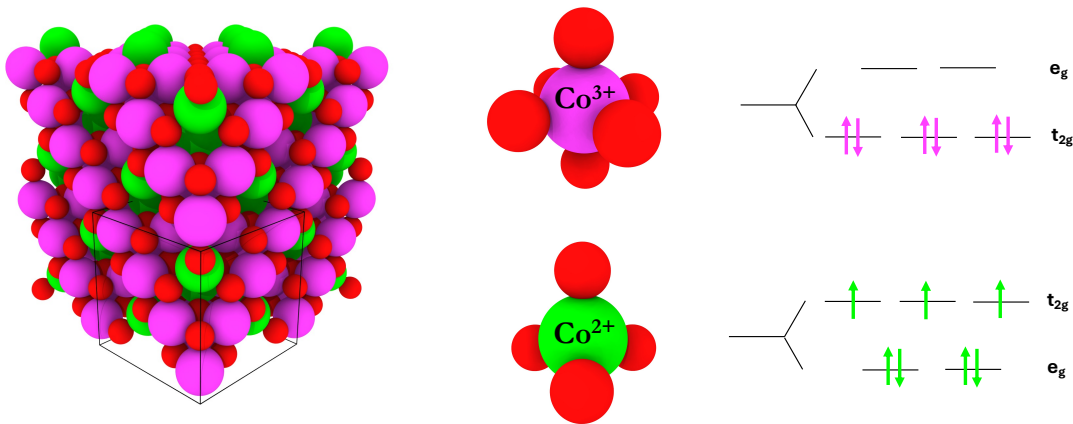


FIG. 1: Co₃O₄ spinel ($2 \times 2 \times 2$) supercell. Co²⁺ cations (green) occupy tetrahedral sites and Co³⁺ cations (purple) occupy octahedral sites. The right side of the figure illustrates the corresponding crystal-field splittings: the lower-right diagram shows tetrahedrally coordinated Co²⁺ in a d^7 configuration, and the upper-right diagram shows octahedrally coordinated Co³⁺ in a d^6 configuration in the low-spin state.

aqueous environment on Co₃O₄ catalysis remains ambiguous, as both promoting and deactivating effects have been reported in computational²⁶ and experimental^{13,25} studies. Another open question is the actual state of Co₃O₄ under these conditions. Often, one starts from a “fresh” sample and assumes the catalyst remains relatively stable during the catalytic process. However, questions such as how the local structure, oxidation state, and magnetic state of Co₃O₄ change during the catalytic reaction have not yet been thoroughly answered.

On the other hand, oxygen vacancies (V_O) in Co₃O₄ are widely considered important for enhanced catalytic activity^{27–32}, since they can increase the Co²⁺/Co³⁺ ratio and create sites that are more easily oxidized or reduced during the reaction cycle. However, most of these conclusions are based on gas-phase reactions or static models that do not address the stability of vacancy-induced Co²⁺ species under liquid-phase oxidation conditions.

For these reasons, in this work, we combined theoretical and experimental approaches to (i) identify the local electronic and magnetic response to a single V_O in Co₃O₄, (ii) examine its stability at room temperature, and (iii) correlate these states with O K-edge measurements on fresh and post-reaction samples tested in the liquid-phase ethylene glycol oxidation, to further clarify the actual role of oxygen vacancies in this particular catalytic process. It should be noted that this work does not focus on the mechanistic aspects of ethylene glycol oxidation in the liquid phase, and the interested reader is referred to the literature for detailed mechanistic studies^{25,33,34}.

The structure of this work is as follows. First, we present DFT results for ideal Co₃O₄ and for Co₃O₄ containing an oxygen vacancy, analyzing the changes in magnetic moments, density of states, and charge-density differences. We then use *ab initio* molecular dynamics

to test the finite-temperature stability of the vacancy-induced Co²⁺ sites. Finally, we compare the calculated X-ray absorption spectra (O K-edge and Co K-edge) with the experimental spectra of fresh and post-reaction samples and discuss the implications for vacancy creation or healing under liquid-phase oxidation conditions.

II. COMPUTATIONAL DETAILS

All electronic structure calculations, *ab initio* molecular dynamics simulations, and X-ray absorption spectroscopy calculations were carried out using the Vienna *Ab initio* Simulation Package (VASP)^{35,36} (version 6.3.2) within the framework of spin-polarized density functional theory (DFT). Exchange–correlation effects and long-range dispersion interactions were described by the optPBE-vdW functional^{37–39}. On-site Coulomb interactions among the Co $3d$ electrons were treated within the DFT+ U formalism of Dudarev *et al.*⁴⁰, employing an effective Hubbard parameter of $U_{\text{eff}} = 2.43$ eV. We have shown previously that the aforementioned setting can reproduce the electronic and structural properties of Co₃O₄ in good agreement with experimental and theoretical data⁴¹.

The interaction between valence electrons and ionic cores was represented by the Projector Augmented Wave (PAW) method⁴², as implemented by Kresse and Joubert^{36,43}. Plane-wave expansions were performed with a kinetic energy cutoff of 500 eV. The Brillouin zone was sampled using a Monkhorst–Pack grid of $5 \times 5 \times 5$ \mathbf{k} -points for bulk Co₃O₄. The bulk Co₃O₄ model contained 56 atoms in a cubic supercell of approximately $8 \times 8 \times 8 \text{ \AA}^3$ (see Ref.^{41,44}). Gaussian smearing of 0.1 eV was applied for partial occupancies, and non-spherical contributions inside the PAW spheres were included. Electronic self-consistency was reached when the total energy difference

between successive iterations was below 10^{-6} eV.

Ab initio molecular dynamics (AIMD) simulations of the bulk Co_3O_4 were performed in the *NPT* ensemble using a Langevin thermostat⁴⁵. The target temperature was held at $T = 300$ K. A time step of $\Delta t = 0.5$ fs was used for $N_{\text{step}} = 100,000$ steps, yielding a total trajectory length of 50 ps. Forces and stresses were evaluated at each step with the same electronic settings as above. The trajectories were generated at the Γ point.

The O K-edge and Co K-edge X-ray absorption spectra were computed on top of the converged spin-polarized DFT+*U* calculations described above. For both edges we employed a core-excited final-state approach within VASP⁴⁶, in which the absorbing atom is replaced by a PAW potential containing a 1s core hole, while all other atoms retain the ground-state potentials. The same optPBE-vdW functional, $U_{\text{eff}} = 2.43$ eV, and plane-wave cutoff as in the ground-state calculations were used to ensure consistency. In order to minimize spurious interaction between periodic images of the core hole, the XAS was evaluated in the 56-atom Co_3O_4 supercell, and the core hole was placed on the site of interest, i.e., lattice O or Co in octahedral/tetrahedral coordination.

Following recent theoretical XANES studies of Co_3O_4 at the O K-edge¹¹ and at the Co K-edge⁴⁷, the calculated spectra were post-processed by convolution with an energy-dependent Lorentzian to account for core-hole lifetime broadening and inelastic losses, and an additional Gaussian of constant width to mimic the experimental energy resolution. A rigid energy shift was then applied so that the intense pre-edge/edge feature of the calculated spectra coincides with the corresponding experimental peak. The spectra were baseline-corrected and normalized to unity in a common post-edge energy window, consistent with the experimental normalization to the edge jump. For more details on these post-processing steps, the interested reader is referred to the above papers. For the Co K-edge, separate spectra were computed for tetrahedral Co^{2+} and octahedral Co^{3+} sites and combined in the stoichiometric ratio of 1:2 ($\text{Co}_{\text{tet}}^{2+}:\text{Co}_{\text{oct}}^{3+}$), using the same broadening, alignment, and normalization protocol for all ideal and vacancy-containing configurations.

III. EXPERIMENTAL DETAILS

Liquid-phase ethylene glycol oxidation The experiments were performed in a batch reactor (Büchi) made of Hastelloy C-22, resistant to highly alkaline conditions. Catalytic reactions were conducted at 120°C under aerobic conditions (10 bar O_2) with 0.65 M KOH and 0.025 M or 0.325 M ethylene glycol (EG) for 6 h. Further details of Co_3O_4 synthesis procedure by co-precipitation, SBA-15 hard-templated and spray-flame can be found in earlier publications.^{25,48-50} Standard characterization of the as-synthesized and post-catalysis of the hard-templated Co_3O_4 samples, and of further catalytic ac-

tivity determination can be found in a previous study²⁵.

X-ray absorption spectroscopy The O K-edge and Co $L_{2,3}$ -edges X-ray absorption spectroscopy measurements were performed at the UE46-PGM1⁵¹ beamline at the synchrotron BESSY II. The measurements at the O K-edge have been carried out in the total electron yield (TEY) mode with linear horizontally polarized X-rays, while the Co $L_{2,3}$ -edges (shown in Figure S2) were measured with circular polarized X-rays. The absorption coefficient was calculated using the signal of the photocurrent divided by the monitor signal. The sample background was corrected by subtraction with a linear function applied in the pre-edge region of the data. Afterwards, the data was normalized with respect to the edge jump. The experimental data shown in Figure 6 are the result of two averaged scans for each sample.

The Co K-edge XAS measurements⁵² were performed at the SAMBA beamline of the SOLEIL synchrotron, operating with an electron beam current of 450 mA. The incident energy was selected by a Si (200) double crystal monochromator. Incident flux was ca. 1×10^{10} ph/s using a beam size of 1×1 mm. The Mn and Co K-edges were utilized to conduct measurements in transmission mode. The samples were prepared by diluting the corresponding powder with cellulose in a pellet ($\varnothing = 13$ mm), followed by placement in the sample holder and sealing with Kapton tape. Calibration was performed using Mn and Co metal foils. The final spectra were normalized and processed using the Fastosh software (for more details, see Ref.⁵²).

Magnetometry The magnetic properties were recorded with the vibrating sample magnetometer (VSM) option of a Quantum Design PPMS DynaCool. Temperature-dependent $M(T)$ magnetization curves were recorded with the zero field cooled - field cooled (ZFC-FC) protocol between 5 and 300 K with an applied magnetic field of 0.1 T.

IV. RESULTS AND DISCUSSION

A. Oxygen Vacancies in Bulk Co_3O_4

1. DFT Calculations at 0 K

First, DFT calculations for ideal Co_3O_4 were carried out and used as the reference throughout this work. They reproduce the expected antiferromagnetic ground state and gives a local magnetic moment of about $2.6 \mu_B$ for the tetrahedral Co^{2+} sites and $0 \mu_B$ for the octahedral Co^{3+} sites (see Table S1 in the Supporting Information). The optimized lattice constant obtained with the present DFT setup is 8.156 Å and the band gap is 1.61 eV, both in good agreement with experimental reports^{19,23,53,54} and consistent with previous DFT studies that are relevant to this work^{11,47}. A more detailed validation of the accuracy of the current DFT settings is provided in Ref. 41.

Similar DFT calculations were performed for Co_3O_4

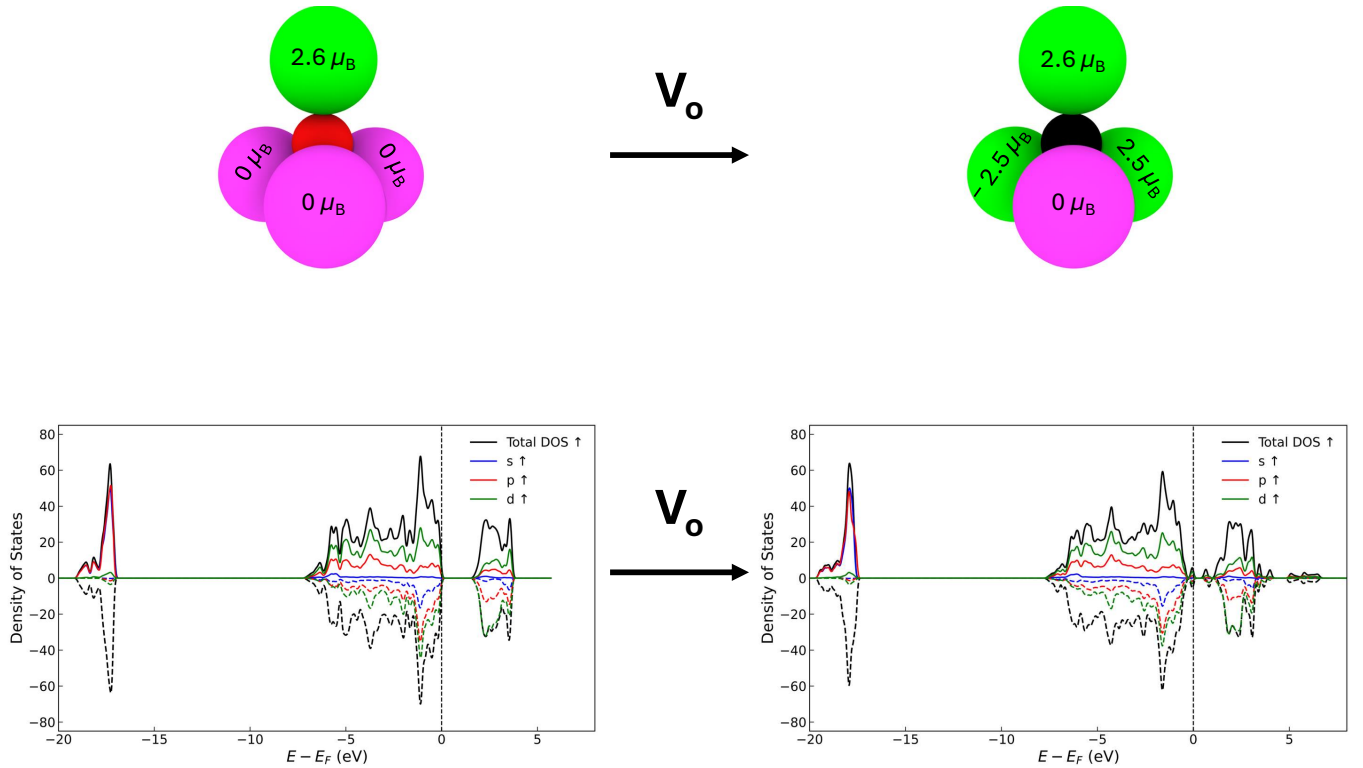


FIG. 2: Local structural and electronic response of Co_3O_4 to the creation of an oxygen vacancy. Top: atomic configuration around the O site before (left) and after (right) removing the central lattice O atom. In the ideal case, the O atom is coordinated to three low-spin Co^{3+} (purple, $0 \mu_B$) and one high-spin Co^{2+} (green, $2.6 \mu_B$). After introducing the O vacancy, two of the neighboring Co^{3+} ions are reduced to Co^{2+} , as indicated by their change to green and the appearance of finite magnetic moments, demonstrating local charge and spin redistribution. Bottom: spin-resolved, orbital-projected density of states (s, p, d) summed over all atoms. Solid lines denote the spin-up channel and dashed lines of the same color denote the spin-down channel (only spin-up is listed in the legend). In ideal Co_3O_4 a clear band gap is present. After the vacancy is created, additional Co $3d$ character appears closer to the Fermi level, spin splitting becomes visible, and the band gap is narrowed.

containing a single oxygen vacancy. A comparison of the results with the ideal Co_3O_4 case is shown in Figure 2. In the upper panels, the local atomic environment around the oxygen site is shown before and after removing the O atom. In the ideal structure (left), one O atom is coordinated to four Co atoms: three are Co^{3+} (purple) with $0 \mu_B$ and one is Co^{2+} (green) with $2.6 \mu_B$. After introducing the oxygen vacancy (right), two of the Co^{3+} cations adjacent to the vacancy are reduced to Co^{2+} , which are highlighted by the appearance of local magnetic moments (and are shown in green). This indicates that removing a single O atom redistributes charge and spin in the neighborhood of the vacancy, converting previously nonmagnetic, low-spin Co^{3+} sites into high-spin Co^{2+} sites. In addition, the two newly formed high-spin Co^{2+} ions adopt opposite spin directions. Table S2 in the supporting information provides the detailed orbital-resolved spin moments (s, p, d) and the resulting total

local magnetic moment for every ion in the Co_3O_4 supercell. It may be worth adding that the existence of a finite X-ray magnetic circular dichroism (XMCD) signal, as shown in Figure S2, may also be attributed to the uncompensated moments that arise when the Co^{2+} ions adopt a high-spin configuration.

The lower part of Fig. 2 shows the spin-resolved, orbital-projected density of states (DOS) for the two cases. The DOS is decomposed into s , p , and d contributions. For each orbital the spin-up component is shown as a solid line, while the corresponding spin-down component is shown as a dashed line (only the spin-up curves are listed in the legend, but each has a dashed counterpart in the plot). For the ideal Co_3O_4 structure, the DOS displays a clear band gap and the d states around the Fermi level are nearly spin-compensated, which is consistent with low-spin Co^{3+} . After introducing the oxygen vacancy, additional d -character appears closer to

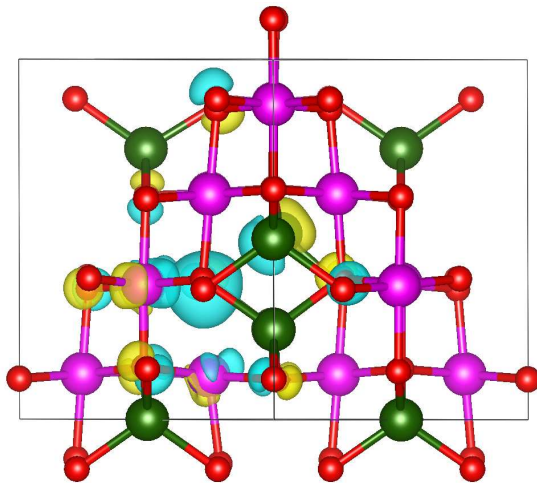


FIG. 3: Charge density difference $\Delta\rho = \rho_{V_O} - \rho_{\text{ideal}}$ for Co_3O_4 with a single oxygen vacancy. Cyan isosurfaces indicate negative charge depletion at the vacancy site and along the former Co–O bonds, while yellow isosurfaces show negative charge accumulation on neighboring Co cations and nearby O atoms, showing redistribution of the electrons left behind by the removed oxygen.

the Fermi level and the spin-up and spin-down d curves no longer perfectly overlap; this is indicative of the reduction of neighboring Co^{3+} to high-spin Co^{2+} and the associated local spin polarization. At the same time, the onset of unoccupied states shifts so that the band gap is narrowed compared to the ideal case.

Figure 3 shows the charge density difference (CDD) $\Delta\rho = \rho_{V_O} - \rho_{\text{ideal}}$ for Co_3O_4 after removing one lattice oxygen atom. In this color scheme, cyan denotes electron density *depletion* and yellow denotes electron density *accumulation*. A large cyan lobe is located at the position of the missing O atom and stretches along the former Co–O bonds, confirming that negative charge is removed from that region when the oxygen is taken out. The yellow isosurfaces appear mainly on the neighboring Co cations and along some of the remaining Co–O bonds, which shows where and how the electrons are redistributed. This indicates that due to the O vacancy, electron density is reallocated from the vacancy site itself and transferred to the adjacent Co–O units, thus locally reducing the nearby Co ions and polarizing the surrounding framework.

2. The Role of Finite Temperature

An important question for their role in catalysis is whether the Co^{2+} species next to the oxygen vacancy in the optimized DFT structures remain stable at finite temperatures when the lattice is allowed to fluctuate. In the relaxed V_O structure the two Co atoms adjacent to the vacancy are five-fold coordinated (distorted octahedral) and carry a high-spin moment of about $2.5 \mu_B$. To test the thermal stability of this configuration, we performed an *ab initio* molecular dynamics simulation at

300 K starting from the relaxed V_O structure and propagated the system for 50 ps with a 0.5 fs time step. In the ideal Co_3O_4 unit cell there are eight Co^{2+} sites, and here we label the two vacancy-induced Co^{2+} as Co 9 and Co 10. The analysis is shown in Fig. 4, where the left column (panels (a), (c), (e)) corresponds to Co ion 9 and the right column (panels (b), (d), (f)) corresponds to Co ion 10.

Panels (a) and (b) report the time evolution of the distances between each of these Co atoms and *all* O atoms in the unitcell. In both cases five Co–O distances stay clustered in the 1.9–2.2 Å range for the entire 50 ps trajectory, while all other O atoms remain clearly farther away (> 3 Å). This indicates that neither of the two Co atoms regains a full sixfold octahedral environment, nor does it collapse to adopt a lower coordination. To quantify this, panels (c) and (d) show the corresponding coordination numbers as a function of time, obtained by counting all O atoms within 2.3 Å of the Co ion. For both Co^{2+} sites the coordination number is essentially constant at 5 throughout the trajectory, with only a few very short-lived drops to 4. These brief excursions coincide with a temporary elongation of one Co–O bond across the 2.3 Å cutoff and do not persist. Importantly, we never observe an increase to 6, i.e., no spontaneous reoccupation of the vacant site or rearrangement into a regular octahedron occur at 300 K. We therefore conclude that the vacancy-induced, five-fold coordinated Co^{2+} environment is structurally stable on the 50 ps time scale at room temperature, and that any further structural change would require overcoming a higher barrier than what thermal fluctuations at 300 K can provide.

Panels (e) and (f) track the local magnetic moments of the same two Co ions. Co 9 (panel (e)) retains a nearly constant moment of $\sim -2.5 \mu_B$ over the whole simula-

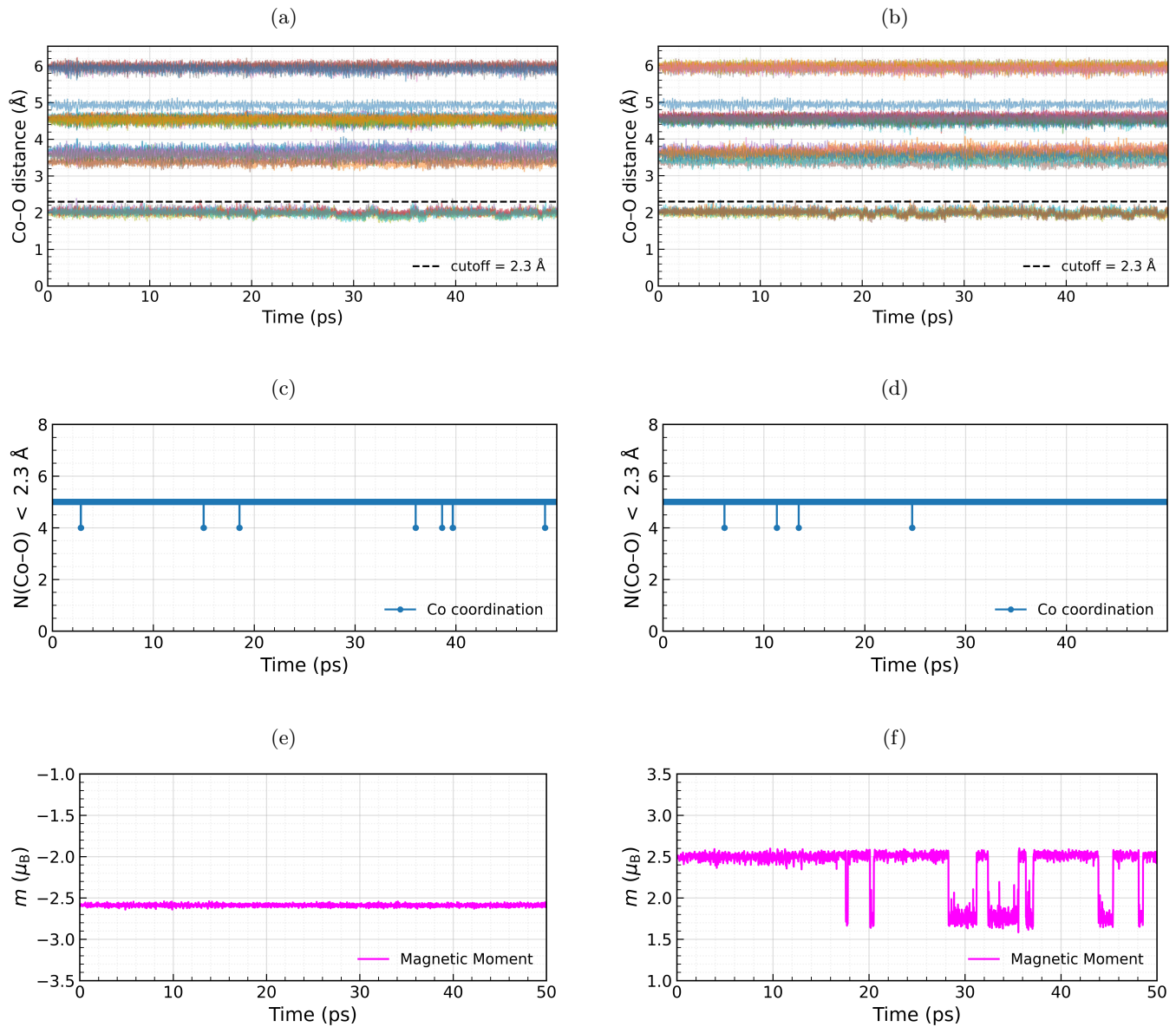


FIG. 4: Time evolution of the two Co ions next to the oxygen vacancy, followed over a 50 ps *ab initio* MD trajectory at 300 K. Panels (a) and (b) track all Co–O distances for Co 9 and Co 10. Each ion holds on to five short Co–O bonds in the range of 1.9–2.2 Å, while all remaining oxygen atoms are found beyond a distance of 3 Å. Neither site ever regains an octahedral environment; the five-fold coordination imposed by the vacancy remains intact. The coordination number plots in panels (c) and (d), obtained by counting O atoms within 2.3 Å cutoff, show the same scenario: both Co^{2+} centers fluctuate around a value of 5, with only momentary drops to 4 and never any increase to reach 6. This configuration is therefore structurally stable at 300 K. Panels (e) and (f) follow the magnetic moments. Co 9 stays essentially locked in its high-spin state at roughly $2.5 \mu_B$ for the entire simulation. Co 10 shows occasional, very short-lived excursions down to 1.6 – $2.0 \mu_B$, but always returns to the same high-spin value, and never displays anything resembling a spin collapse. Overall, these results show that the oxygen vacancy produces two Co^{2+} ions that remain both structurally and magnetically robust over the full 50 ps trajectory at 300 K.

tion, which is exactly the value found in the static DFT calculation and is characteristic of high-spin Co^{2+} . Co 10 (panel (f)) behaves similarly for most of the simulation but exhibits several short intervals in which its moment drops to about 1.6 – $2.0 \mu_B$. These episodes are transient

and the moment always recovers to $\approx 2.5 \mu_B$; at no point does the spin collapse to $\sim 0 \mu_B$, i.e., we do not observe a conversion back to low-spin Co^{3+} . Because the number of Co–O neighbours does not change in a permanent way, these short drops in the magnetic moment cannot be at-

tributed to a change of site or oxidation state. The more plausible explanation is that the Co ion remains Co^{2+} in the same five-fold environment, but thermal motion at 300 K slightly perturbs the local bonds; consequently, the calculated moment briefly decreases before returning to its equilibrium value. Thus, these are small temperature-driven oscillations of the moment rather than a genuine $\text{Co}^{2+} \rightarrow \text{Co}^{3+}$ transition or a structural rearrangement. Overall, the AIMD confirms that the oxygen-vacancy-induced Co^{2+} sites are both *structurally* and *magnetically* robust at 300 K on the 50 picoseconds time scale. It may be worth noting that electron paramagnetic resonance (EPR) studies on Co_3O_4 platelets used for the partial oxidation of cinnamyl alcohol have likewise reported a surface-near distorted high-spin Co^{2+} center, tentatively attributed to a distorted octahedral or tetrahedral site.³²

B. Liquid-Phase Ethylene Glycol Oxidation

1. Catalytic Activity, Selectivity, Reusability, and the impact of O_2 Pressure

Figure 5 summarizes the relation between O_2 pressure as well as catalyst reusability for the activity and selectivity of the hard-templated Co_3O_4 samples during liquid-phase ethylene glycol oxidation. The left part of the figure shows the ethylene glycol conversion and the yields of glycolic acid (GA), formic acid (FA), and oxalic acid (OA) after 6 h at 120 °C, 0.325 M EG, and 0.65 M KOH for O_2 pressures of 5, 10, and 15 bar. The total height of each bar corresponds to the overall EG conversion; the colored segments show the individual yields of GA, FA, and OA, respectively. By increasing the O_2 pressure, the ethylene glycol conversion and the absolute yields of the oxidation products increase. The selectivity pattern changes only moderately: the glycolic acid (GA) yield does not increase substantially with increasing O_2 pressure, while the relative contributions of formic acid (FA) and oxalic acid (OA) are enhanced, i.e., at higher O_2 pressure, more strongly oxidized products are favored.

The right part of Figure 5 shows the conversion and product yields for three consecutive reaction cycles, which are carried out at 10 bar O_2 under the same alkaline conditions. Both overall conversion and the relative distribution among GA, FA, and OA remain mainly unchanged in consecutive cycles. Thus, it can be suggested that the hard-templated Co_3O_4 catalyst is not only active and selective but also structurally stable and reusable under the alkaline, O_2 -rich liquid-phase reaction environment. Further details on the aforementioned experiments can be found in a recent publication²⁵.

2. X-ray Absorption Spectroscopy

O K-edge X-ray Absorption Spectroscopy:

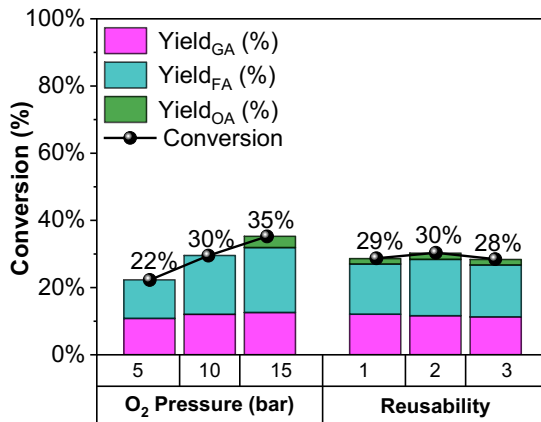


FIG. 5: Effect of O_2 pressure and catalyst reusability for the hard-templated Co_3O_4 sample in the liquid-phase oxidation of ethylene glycol. The left part shows the EG conversion and the corresponding yields/selectivities of glycolic acid (GA), formic acid (FA), and oxalic acid (OA) after 6 h at 120 °C, 0.325 M EG, and 0.65 M KOH for O_2 pressures of 5, 10, and 15 bar. The right part shows EG conversion and GA/FA/OA yields/selectivities for three consecutive runs at 10 bar O_2 under the same conditions, which illustrates the stability and reusability of the hard-templated sample.

Figure 6 shows the evolution of the O K-edge of Co_3O_4 for the hard-templated sample (HT) and how this evolution compares with our theoretical reference spectra. Panel (a) corresponds to the HT sample and contains three curves: the fresh catalyst (blue), the 0.025 EG post reaction spectrum (orange), and the 0.325 EG post reaction spectrum (red). Panel (b) shows the theoretical O K-edge for the ideal Co_3O_4 structure (black) and for Co_3O_4 containing a single oxygen vacancy (blue). Although the discussion in this work focuses on the HT sample, the corresponding experimental spectra for the spray flame synthesized (SF) and co-precipitated (CP) samples, which exhibit the same trends, are also provided in the Supporting Information (Figure S1).

For the HT sample the trend is the same as for the other two catalysts. The fresh material has a slightly weaker intensity at the onset of the absorption, that is in the first and second features of the O K-edge at 531 eV and 543 eV, respectively. After reaction, the spectra sharpen and the intensities at both the 531 eV peak and 543 eV rise. This effect is most pronounced for the 0.325 EG post reaction state. The SF and CP samples follow the same behavior, as shown in Figure S1, therefore all three synthesis routes lead to catalysts that move in the same spectral direction when they are exposed to the liquid-phase ethylene glycol oxidation conditions.

The comparison with the calculated spectra in panel (b) makes this interpretation quantitative. In the calculation, the ideal Co_3O_4 has two relatively strong and well separated low energy features, because the O 2p

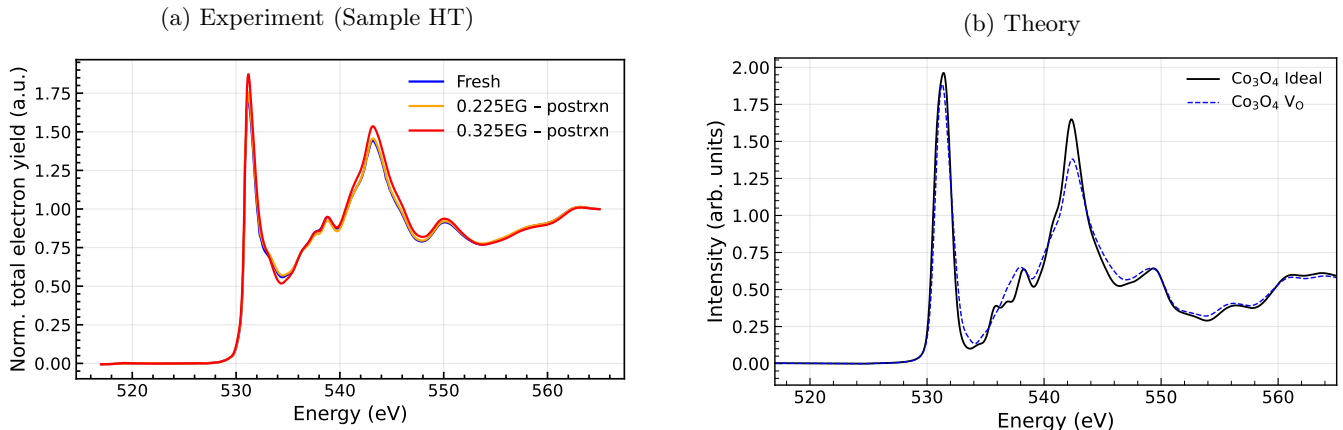


FIG. 6: O K-edge X-ray absorption spectra (XAS) of Co_3O_4 for the hard-templated sample (HT) before and after liquid-phase ethylene glycol oxidation, compared with theoretical reference spectra. Panel (a) shows the experimental spectra for the fresh catalyst (blue), the 0.025 EG post-reaction state (orange), and the 0.325 EG post-reaction state (red). Panel (b) displays the theoretical O K-edge spectra for the ideal Co_3O_4 spinel (black) and for a structure containing a single oxygen vacancy (blue). The reduced intensity of the first two peaks in the vacancy-containing system closely resembles the experimental fresh-state spectrum, while the ideal calculated spectrum matches the oxidized 0.325 EG post-reaction data. The same spectral trend is observed for the SF and CP samples (see Figure S1), all of which indicates that oxygen-vacancy-type defects are healed.

states are strongly hybridized with Co $3d$ states in a fully oxidized spinel environment. When an oxygen vacancy is introduced, the theoretical spectrum loses intensity in exactly those first two features.

The experimental fresh spectrum of HT in panel (a), together with the fresh spectra of SF and CP in Figure S1, resemble this vacancy-like calculated curve, while the 0.325 EG post reaction spectra resemble much more the ideal calculated curve with stronger first and second peaks at 531 eV and 543 eV, respectively. In other words, the catalytically treated samples evolve from a vacancy-perturbed O K-edge toward an almost ideal spinel-like O K-edge. Therefore, one may deduce that this correspondence between experiment and theory supports that the liquid-phase reaction heals oxygen-vacancy-type defects and restores a more oxidized Co–O electronic structure. In other words, it can be suggested that there is a redox competition: ethylene glycol reduces the surface, while O_2 in the reaction atmosphere reoxidizes it. This is further supported by the observation that higher O_2 pressure leads to higher conversion, and that the catalyst remains relatively stable and reusable over multiple reaction cycles (see Section IV B 1).

Co K-edge X-ray Absorption Spectroscopy:

Figure 7 shows the Co K-edge XANES of Co_3O_4 together with the site-resolved calculated spectra and their weighted sums. The experimental spectrum of the fresh hard-templated sample⁵² is shown in red and serves as the reference (Co K-edge XAS for the post-reaction samples are not yet available at the time of this publication). The calculated spectra for octahedral Co^{3+} and tetrahedral Co^{2+} in the *ideal* spinel, together with their

stoichiometric weighted average, reproduce very well the edge position and the shape of the main rising feature in the experiment. As expected, the Co^{2+} curve is slightly lower in energy, the Co^{3+} curve is slightly higher and steeper, and the “ideal” (weighted avg) spectrum lies between them, approaching the experimental curve.

The same site-by-site construction was then carried out for the structure containing an oxygen vacancy. In this case, the “ V_O ” (weighted avg) spectrum is slightly shifted toward lower energy and the edge is a bit less steep. Both effects are what one would expect if the vacancy locally increases the Co^{2+} character. The change, however, is modest: the V_O and ideal weighted spectra remain close, but the direction of the change is consistent with the density of states (DOS), charge density difference (CDD), and O K-edge results, which all indicate a vacancy-induced local reduction. In other words, the way the V_O spectrum shifts to slightly lower energy while getting broader, is fully consistent with the previously suggested picture that an oxygen vacancy leads to more Co^{2+} character.

3. Magnetometry

In addition, magnetometry measurements have been performed on the hard-templated sample for the fresh and post-catalysis samples as a function of temperature (see Fig. S3). Using the Curie-Weiss law, the temperature-dependent magnetization allows the calculation of the Curie constant and therefore the effective magnetic moment of the sample μ_{eff} as described in Mu-

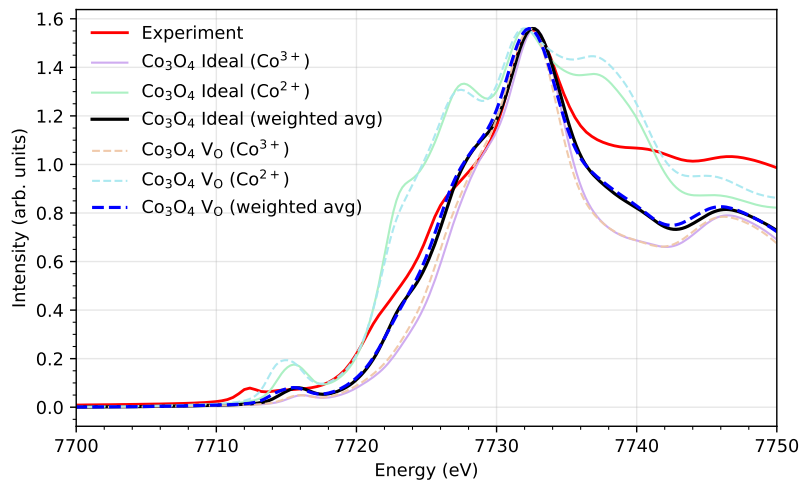


FIG. 7: Co K-edge XANES of Co_3O_4 compared with site-resolved theoretical spectra. The experimental spectrum of the fresh hard-templated sample⁵² (red) serves as the reference. Calculated spectra for octahedral Co^{3+} and tetrahedral Co^{2+} , along with their stoichiometric weighted average, reproduce the experimental spectra with excellent agreement. For the Co_3O_4 with the V_O , the weighted spectrum exhibits a slight shift toward lower energy and a less steep edge, which suggests an increased Co^{2+} character. This modest but consistent change supports the interpretation of vacancy-induced local reduction, in agreement with density of states (DOS), charge density difference (CDD), and O K-edge analyses as previously discussed.

giraneza et al.⁵⁵. Between the fresh sample and the two post-catalysis samples an average reduction of 5% of μ_{eff} was observed. Considering that in Co_3O_4 only Co^{2+} contributes to the effective magnetic moment, the magnetometry results indicate that the Co^{2+} amount is reduced after catalysis, which is in agreement with the statements in the previous section regarding oxygen refilling and the oxidation of Co^{2+} to Co^{3+} .

V. CONCLUSIONS

In the present work, we investigated oxygen vacancies in Co_3O_4 both in the bulk phase and under liquid-phase ethylene glycol oxidation by combining spin-polarized DFT+ U , *ab initio* molecular dynamics, and theoretical and experimental X-ray absorption spectroscopy (O and Co K-edge). Our main findings can be summarized as follows:

1. Introducing a single V_O into ideal bulk Co_3O_4 reduces two neighboring octahedral Co^{3+} ions to high-spin Co^{2+} and narrows the band gap.
2. These newly formed Co^{2+} ions adopt similar local magnetic moments ($\sim 2.5 \mu_\text{B}$) but in opposite directions.
3. They do not move into regular tetrahedral positions but remain in vacancy-perturbed, distorted octahedral environments with five-fold coordination.
4. *Ab initio* MD at 300 K (50 ps) shows that both vacancy-induced Co^{2+} sites remain stable, struc-

turally (the Co–O coordination stays at 5 with only brief fluctuations) and magnetically (the local moments stay in the $\sim 2.5 \mu_\text{B}$ Co^{2+} range). This suggests that any further structural transformation would require overcoming a higher activation barrier than what is accessible at 300 K in our simulations.

5. Comparison of the computed O K-edge spectra for ideal Co_3O_4 and for Co_3O_4 with V_O to the experimental O K-edge spectra of the as-prepared and post-reaction catalysts shows that the fresh samples resemble the vacancy-containing calculation, while the spectra after liquid-phase ethylene glycol oxidation shift toward the ideal computed spectrum. This suggests that the reaction conditions tend to refill or heal oxygen-vacancy-type defects and drive the catalyst back toward a more oxidized, spinel-like state.
6. Consistently, magnetometry shows an average reduction of 5% in effective magnetic moment after catalysis, suggesting a lower Co^{2+} content.
7. This picture is further supported by the fact that higher O_2 pressures enhance EG conversion and that the catalyst remains stable and active across multiple reaction cycles.

ACKNOWLEDGMENTS

We are grateful for funding by the Deutsche Forschungsgemeinschaft (DFG, German Research Foundation) in CRC/TRR 247 (project-ID 388390466: projects A01, A10 and B02) and under Germany's Excellence Strategy – EXC 2033 RESOLV (project-ID 390677874). The authors also acknowledge the computing time provided to them by the Paderborn Center for Parallel Computing (PC2). The authors thank the Helmholtz-Zentrum Berlin für Materialien und Energie for the allocation of synchrotron radiation beamtime within proposal ST-242-12862 at the synchrotron BESSY II and financial support for travel to BESSY II. Special thanks to Leon Müller and Christof Schulz for the

spray-flame synthesized samples. Similarly to Carsten Placke-Yan and Stephan Schulz for the synthesis of coprecipitation samples. We acknowledge SOLEIL for the provision of synchrotron radiation facilities and would like to thank Dr. G. Landrot and the other beamline scientists for their assistance in using the SAMBA beamline (proposal no. 20240233).

DATA AVAILABILITY

The data generated and analyzed during the current study are available from the corresponding authors upon request.

-
- ¹ Waidhas, F.; Haschke, S.; Khanipour, P.; Fromm, L.; Görling, A.; Bachmann, J.; Katsounaros, I.; Mayrhofer, K. J.; Brummel, O.; Libuda, J. Secondary Alcohols as Rechargeable Electrofuels: Electrooxidation of Isopropyl Alcohol at Pt Electrodes. *ACS Catal.* **2020**, *10*, 6831–6842.
 - ² Hill, C. K.; Hartwig, J. F. Site-selective oxidation, amination and epimerization reactions of complex polyols enabled by transfer hydrogenation. *Nat. Chem.* **2017**, *9*, 1213–1221.
 - ³ Finocchio, E.; Willey, R. J.; Busca, G.; Lorenzelli, V. FTIR studies on the selective oxidation and combustion of light hydrocarbons at metal oxide surfaces Part 3.—Comparison of the oxidation of C₃ organic compounds over Co₃O₄, MgCr₂O₄ and CuO. *J. Chem. Soc., Faraday Trans.* **1997**, *93*, 175–180.
 - ⁴ Anke, S.; Bendt, G.; Sinev, I.; Hajiyani, H.; Antoni, H.; Zegkinoglou, I.; Jeon, H.; Pentcheva, R.; Roldan Cuenya, B.; Schulz, S.; others Selective 2-propanol oxidation over unsupported Co₃O₄ spinel nanoparticles: mechanistic insights into aerobic oxidation of alcohols. *ACS Catal.* **2019**, *9*, 5974–5985.
 - ⁵ Doheim, M.; El-Shobaky, H. Catalytic conversion of ethanol and iso-propanol over ZnO-treated Co₃O₄/Al₂O₃ solids. *Colloids Surf.* **2002**, *204*, 169–174.
 - ⁶ Yang, T.; Kastenmeier, M.; Ronovský, M.; Fusek, L.; Skála, T.; Waidhas, F.; Bertram, M.; Tsud, N.; Matviya, P.; Prince, K. C.; others Selective electrooxidation of 2-propanol on Pt nanoparticles supported on Co₃O₄: an in-situ study on atomically defined model systems. *J. Phys. D* **2021**, *54*, 164002.
 - ⁷ Omranpoor, A. H.; Bera, A.; Bullert, D.; Linke, M.; Salamon, S.; Webers, S.; Wende, H.; Hasselbrink, E.; Spohr, E.; Kenmoe, S. 2-Propanol interacting with Co₃O₄ (001): A combined vSFS and AIMD study. *J. Chem. Phys.* **2023**, *158*.
 - ⁸ Anke, S.; Falk, T.; Bendt, G.; Sinev, I.; Haevecker, M.; Antoni, H.; Zegkinoglou, I.; Jeon, H.; Knop-Gericke, A.; Schlögl, R.; others On the reversible deactivation of cobalt ferrite spinel nanoparticles applied in selective 2-propanol oxidation. *J. Catal.* **2020**, *382*, 57–68.
 - ⁹ Douma, D. H.; Nono, K. N.; Omranpoor, A. H.; Lamperti, A.; Debernardi, A.; Kenmoe, S. Probing the local environment of active sites during 2-propanol oxidation to acetone on the Co₃O₄ (001) surface: Insights from first-principles O K-edge XANES spectroscopy. *J. Phys. Chem. C* **2023**, *127*, 5351–5357.
 - ¹⁰ Omranpoor, A.; Kox, T.; Spohr, E.; Kenmoe, S. Influence of temperature, surface composition and electrochemical environment on 2-propanol decomposition at the Co₃O₄ (001)/H₂O interface. *Appl. Surf. Sci. Advances* **2022**, *12*, 100319.
 - ¹¹ Kenmoe, S.; Douma, D. H.; Raji, A. T.; M'Passi-Mabiala, B.; Götsch, T.; Girgsdies, F.; Knop-Gericke, A.; Schlögl, R.; Spohr, E. X-ray Absorption Near-Edge Structure (XANES) at the O K-Edge of Bulk Co₃O₄: Experimental and Theoretical Studies. *Nanomaterials* **2022**, *12*, 921.
 - ¹² Omranpoor, A. H.; Kenmoe, S. 2-Propanol Activation on the Low Index Co₃O₄ Surfaces: A Comparative Study Using Molecular Dynamics Simulations. *Catalysts* **2023**, *14*, 25.
 - ¹³ Falk, T.; Budiyanto, E.; Dreyer, M.; Pflieger, C.; Wafel, D.; Büker, J.; Weidenthaler, C.; Ortega, K. F.; Behrens, M.; Tüysüz, H.; others Identification of active sites in the catalytic oxidation of 2-propanol over Co_{1+x}Fe_{2-x}O₄ spinel oxides at solid/liquid and solid/gas interfaces. *ChemCatChem* **2021**, *13*, 2942–2951.
 - ¹⁴ Feizi, H.; Bagheri, R.; Song, Z.; Shen, J.-R.; Al-lakhverdiev, S. I.; Najafpour, M. M. Cobalt/cobalt oxide surface for water oxidation. *ACS Sustain. Chem. Eng.* **2019**, *7*, 6093–6105.
 - ¹⁵ Jiao, F.; Frei, H. Nanostructured cobalt oxide clusters in mesoporous silica as efficient oxygen-evolving catalysts. *Angew. Chem.* **2009**, *121*, 1873–1876.
 - ¹⁶ Hu, L.; Peng, Q.; Li, Y. Selective synthesis of Co₃O₄ nanocrystal with different shape and crystal plane effect on catalytic property for methane combustion. *J. Am. Chem. Soc.* **2008**, *130*, 16136–16137.
 - ¹⁷ Xie, X.; Li, Y.; Liu, Z.-Q.; Haruta, M.; Shen, W. Low-temperature oxidation of CO catalysed by Co₃O₄ nanorods. *Nature* **2009**, *458*, 746–749.
 - ¹⁸ Li, W.-Y.; Xu, L.-N.; Chen, J. Co₃O₄ nanomaterials in lithium-ion batteries and gas sensors. *Adv. Funct. Mater.* **2005**, *15*, 851–857.
 - ¹⁹ Roth, W. The magnetic structure of Co₃O₄. *J. Phys. Chem. Solids* **1964**, *25*, 1–10.

- ²⁰ Cheng, C.-S.; Serizawa, M.; Sakata, H.; Hirayama, T. Electrical conductivity of Co_3O_4 films prepared by chemical vapour deposition. *Mater. Chem. Phys.* **1998**, *53*, 225–230.
- ²¹ Koumoto, K.; Yanagida, H. Electrical Conduction in Pure and Li-Substituted Co_3O_4 . *J. Am. Ceram. Soc.* **1981**, *64*, C–156.
- ²² Kim, K. J.; Park, Y. R. Optical investigation of charge-transfer transitions in spinel Co_3O_4 . *Solid State Commun.* **2003**, *127*, 25–28.
- ²³ Shinde, V.; Mahadik, S.; Gujar, T.; Lokhande, C. Supercapacitive cobalt oxide (Co_3O_4) thin films by spray pyrolysis. *Appl. Surf. Sci.* **2006**, *252*, 7487–7492.
- ²⁴ Najafshirtari, S.; Friedel Ortega, K.; Douthwaite, M.; Pattison, S.; Hutchings, G. J.; Bondue, C. J.; Tschulik, K.; Waffel, D.; Peng, B.; Deitermann, M.; others A perspective on heterogeneous catalysts for the selective oxidation of alcohols. *Chemistry—A European Journal* **2021**, *27*, 16809–16833.
- ²⁵ Leiva-Leroy, C.; Koul, A.; Nkou, F.; Fandre, J. P.; Ha-reendran, A.; Busser, W.; Tüysüz, H.; Kenmoe, S.; Schuhmann, W.; Muhler, M. From Heat to Electrons: Bridging Heterogeneous Liquid-Phase Thermal and Electrocatalytic Oxidation of Ethylene Glycol over Co_3O_4 . *ChemRxiv* **2025**,
- ²⁶ Wang, H.-F.; Kavanagh, R.; Guo, Y.-L.; Guo, Y.; Lu, G.-Z.; Hu, P. Structural origin: water deactivates metal oxides to CO oxidation and promotes low-temperature CO oxidation with metals. *Angew. Chem. Int. Ed.* **2012**, *51*, 6657–6661.
- ²⁷ Liu, Y.; Peng, Y.; Naschitzki, M.; Gewinner, S.; Schöllkopf, W.; Kühlenbeck, H.; Pentcheva, R.; Roldan Cuenya, B. Surface oxygen vacancies on reduced Co_3O_4 (100): superoxide formation and ultra-low-temperature CO oxidation. *Angewandte Chemie International Edition* **2021**, *60*, 16514–16520.
- ²⁸ Xu, L.; Jiang, Q.; Xiao, Z.; Li, X.; Huo, J.; Wang, S.; Dai, L. Plasma-engraved Co_3O_4 nanosheets with oxygen vacancies and high surface area for the oxygen evolution reaction. *Angewandte Chemie* **2016**, *128*, 5363–5367.
- ²⁹ Ferstl, P.; Mehl, S.; Arman, M. A.; Schuler, M.; Toghan, A.; Laszlo, B.; Lykhach, Y.; Brummel, O.; Lundgren, E.; Knudsen, J.; others Adsorption and activation of CO on Co_3O_4 (111) thin films. *The Journal of Physical Chemistry C* **2015**, *119*, 16688–16699.
- ³⁰ Fung, V.; Tao, F. F.; Jiang, D.-e. General structure–reactivity relationship for oxygen on transition-metal oxides. *The journal of physical chemistry letters* **2017**, *8*, 2206–2211.
- ³¹ Montoya, A.; Haynes, B. S. Periodic density functional study of Co_3O_4 surfaces. *Chem. Phys. Lett.* **2011**, *502*, 63–68.
- ³² Schellenburg, D.; Bihnam, T.; Placke-Yan, C.; Bendt, G.; Prymak, O.; Sato, T.; Jennings, D.; Leiva-Leroy, C.; Zhang, D.; Nachev, M.; others Mechanistic Understanding of Laser-Induced Defect Engineering of Anisotropic Cobalt Oxide Spinel Platelets in Water. *ChemCatChem* **2025**, e01054.
- ³³ Nkou, F. B. S.; Kenmoe, S. Ethylene Glycol Partial Aqueous Oxidation on Co_3O_4 (001) Surfaces: Pathways to Two- and Four-Electron Products in Neutral and Oxidative Conditions. *ChemCatChem* **2025**, *17*, e202401885.
- ³⁴ Nkou, F. B. S.; Kenmoe, S. Ethylene glycol partial oxidation on Co_3O_4 (001) surface: Interplay between solute’s surface coverage and aqueous solvation. *Molecular Catalysis* **2025**, *578*, 114980.
- ³⁵ Kresse, G.; Furthmüller, J. Efficient iterative schemes for ab initio total-energy calculations using a plane-wave basis set. *Phys. Rev. B* **1996**, *54*, 11169.
- ³⁶ Kresse, G.; Furthmüller, J. Efficiency of ab-initio total energy calculations for metals and semiconductors using a plane-wave basis set. *Comput. Mater. Sci.* **1996**, *6*, 15–50.
- ³⁷ Perdew, J. P.; Burke, K.; Ernzerhof, M. Generalized gradient approximation made simple. *Phys. Rev. Lett.* **1996**, *77*, 3865.
- ³⁸ Klimeš, J.; Bowler, D. R.; Michaelides, A. Chemical accuracy for the van der Waals density functional. *J. Condens. Matter Phys.* **2009**, *22*, 022201.
- ³⁹ Klimeš, J.; Bowler, D. R.; Michaelides, A. Van der Waals density functionals applied to solids. *Phys. Rev. B* **2011**, *83*, 195131.
- ⁴⁰ Dudarev, S. L.; Botton, G. A.; Savrasov, S. Y.; Humphreys, C.; Sutton, A. P. Electron-energy-loss spectra and the structural stability of nickel oxide: An LSDA+U study. *Phys. Rev. B* **1998**, *57*, 1505.
- ⁴¹ Omranpour, A.; Behler, J. A high-dimensional neural network potential for Co_3O_4 . *J. Phys.: Condens. Matter* **2024**, *37*, 095701.
- ⁴² Blöchl, P. E. Projector augmented-wave method. *Phys. Rev. B* **1994**, *50*, 17953.
- ⁴³ Kresse, G.; Joubert, D. From ultrasoft pseudopotentials to the projector augmented-wave method. *Phys. Rev. B* **1999**, *59*, 1758.
- ⁴⁴ Omranpour, A.; Behler, J. Insights into the Structure and Dynamics of Water at Co_3O_4 (001) Using a High-Dimensional Neural Network Potential. *arXiv preprint arXiv:2509.00322* **2025**,
- ⁴⁵ Parrinello, M.; Rahman, A. Crystal structure and pair potentials: A molecular-dynamics study. *Physical review letters* **1980**, *45*, 1196.
- ⁴⁶ Karsai, F.; Humer, M.; Flage-Larsen, E.; Blaha, P.; Kresse, G. Effects of electron-phonon coupling on absorption spectrum: K edge of hexagonal boron nitride. *Physical Review B* **2018**, *98*, 235205.
- ⁴⁷ Douma, D. H.; Kenmoe, S. Electronic and Magnetic Properties of Co_3O_4 and $\text{Co}_{3-x}\text{Ni}_x\text{O}_4$ from DFT-Based Simulations of XANES Spectra at the Co K-Edge. *The Journal of Physical Chemistry C* **2024**, *129*, 699–704.
- ⁴⁸ Dong, J.; Song, L.; Yin, J.-J.; He, W.; Wu, Y.; Gu, N.; Zhang, Y. Co_3O_4 nanoparticles with multi-enzyme activities and their application in immunohistochemical assay. *ACS Applied Materials & Interfaces* **2014**, *6*, 1959–1970.
- ⁴⁹ Deng, X.; Chen, K.; Tuysuz, H. Protocol for the nanocasting method: preparation of ordered mesoporous metal oxides. *Chemistry of Materials* **2017**, *29*, 40–52.
- ⁵⁰ Schulz, C.; Dreier, T.; Fikri, M.; Wiggers, H. Gas-phase synthesis of functional nanomaterials: Challenges to kinetics, diagnostics, and process development. *Proceedings of the Combustion Institute* **2019**, *37*, 83–108.
- ⁵¹ Weschke, E.; Schierle, E. The UE46 PGM-1 beamline at BESSY II. *Journal of large-scale research facilities JLSRF* **2018**, *4*, A127.
- ⁵² Fandré, J. P.; Budiayanto, E.; Kumar, A.; Tüysüz, H. Unveiling the Role of Manganese Substitution in Nanocast Cobalt Oxide for Alkaline Water Electrolysis Performance. *ChemCatChem* **2025**, e01178.
- ⁵³ Zasada, F.; Piskorz, W.; Sojka, Z. Cobalt spinel at various redox conditions: DFT+U investigations into the structure and surface thermodynamics of the (100) facet. *J. Phys.*

Chem. C **2015**, *119*, 19180–19191.

- ⁵⁴ Liu, X.; Prewitt, C. T. High-temperature X-ray diffraction study of Co_3O_4 : Transition from normal to disordered spinel. *Phys. Chem. Miner.* **1990**, *17*, 168–172.
- ⁵⁵ Mugiraneza, S.; Hallas, A. M. Tutorial: a beginner's guide to interpreting magnetic susceptibility data with the Curie-Weiss law. *Communications Physics* **2022**, *5*, 95.

Supplementary Information: A Combined Theoretical and Experimental Study of Oxygen Vacancies in Co_3O_4 for Liquid-Phase Oxidation Catalysis

Amir Omranpour,^{1,2,*} Lea Kämmerer,³ Catalina Leiva-Leroy,⁴ Anna Rabe,³ Takuma Sato,⁵ Soma Salamon,³ Joachim Landers,³ Benedikt Eggert,³ Eugen Weschke,⁶ Jean Pascal Fandré,⁷ Ashwani Kumar,⁷ Harun Tüysüz,^{7,8} Martin Muhler,⁴ Heiko Wende,³ and Jörg Behler^{1,2}

¹*Lehrstuhl für Theoretische Chemie II, Ruhr-Universität Bochum, 44780 Bochum, Germany*

²*Research Center Chemical Sciences and Sustainability, Research Alliance Ruhr, 44780 Bochum, Germany*

³*Faculty of Physics and Center for Nanointegration Duisburg-Essen (CENIDE), University of Duisburg-Essen, 47057 Duisburg, Germany*

⁴*Laboratory of Industrial Chemistry, Ruhr-Universität Bochum, 44780 Bochum, Germany*

⁵*Max Planck Institute for Chemical Energy Conversion, 45470 Mülheim an der Ruhr, Germany*

⁶*Helmholtz-Zentrum Berlin für Materialien und Energie (HZB), 12489 Berlin, Germany*

⁷*Heterogeneous Catalysis and Sustainable Energy, Max-Planck-Institut für Kohlenforschung, Kaiser-Wilhelm-Platz 1, 45470 Mülheim an der Ruhr, Germany*

⁸*Catalysis and Energy Materials Group, IMDEA Materials Institute, Calle Eric Kandel 2, 28906, Getafe, Madrid, Spain*

(Dated: November 25, 2025)

I. X-RAY ABSORPTION SPECTROSCOPY

Figure 1 presents additional O K-edge X-ray absorption spectra for the spray flame synthesized (SF) and co-precipitated (CP) Co_3O_4 samples before and after liquid phase ethylene glycol oxidation. The observed spectral changes closely follow those of the hard-templated sample discussed in the main text and confirm that the increased intensity and sharpening of the first two peaks at 0.325 EG indicate a more oxidized Co–O environment across all synthesis routes.

II. X-RAY MAGNETIC CIRCULAR DICHROISM (XMCD)

Figure 2 exemplarily shows the XANES measured at the Co $L_{2,3}$ -edges with the corresponding XMCD for the Co_3O_4 hard-templated (HT) sample after liquid-phase ethylene glycol oxidation with a concentration of 0.325 EG measured at 4 K and an applied magnetic field of 6 T. As suggested by the DFT calculations for the O K-edge, the Co^{3+} ions are reduced to Co^{2+} ions located at the octahedral sites due to oxygen vacancies. Therefore, it can be suggested that uncompensated moments arise as the Co^{2+} ions adopt a high-spin configuration which leads to a finite XMCD signal, as exemplified in Fig. 2.

III. MAGNETOMETRY MEASUREMENTS

Figure 3 (a) shows the temperature-dependent mass magnetization in a range from 5–300 K for the three hard-templated samples before (blue) and after liquid phase

ethylene glycol oxidation (0.025 EG post-reaction (orange) and 0.325 EG post-reaction (red)) under an applied magnetic field of 0.1 T. Using the inverse molar susceptibility χ_{mol} calculated via equation 7 in¹ it is possible to obtain the effective magnetic moment μ_{eff} via the Curie constant by fitting with a linear equation presented in Fig. 3 (b) for the fresh sample. The fit parameters given in panel (b) are rounded to the second decimal. The obtained μ_{eff} show an average reduction of 5% when comparing the fresh sample with the post-catalysis ones ($\mu_{\text{eff}} = 4.33\mu_{\text{B}}$ (Fresh) vs. $\mu_{\text{eff}} = 4.06\mu_{\text{B}}$ (0.025 EG post-reaction) and $\mu_{\text{eff}} = 4.17\mu_{\text{B}}$ (0.325 EG post-reaction)) following the observation of the theoretical calculations that the Co^{2+} amount is reduced after catalysis under the assumption that only Co^{2+} contributes to μ_{eff} in Co_3O_4 .

IV. SITE-RESOLVED MAGNETIC MOMENTS FROM DFT

Tables S1–S3 show the details of the orbital-resolved spin moments (s, p, d) and the resulting total local magnetic moment for every ion in the Co_3O_4 supercell obtained from our DFT calculations.

In all tables, the atoms follow the same ordering:

- ions 1–8 correspond to the tetrahedral Co^{2+} sites,
- ions 9–24 correspond to the octahedral Co^{3+} sites,
- the remaining ions are the O atoms.

This ordering makes it straightforward to assign the expected ~ 2.5 – $2.6 \mu_{\text{B}}$ moments on Co^{2+} , the nearly quenched moments on Co^{3+} , and the small induced moments on oxygen.

Table S1 shows the reference (ideal) Co_3O_4 calculation without an oxygen vacancy. As expected for the normal spinel, the first eight Co atoms (tetrahedral Co^{2+}) carry

* amir.omranpour@rub.de

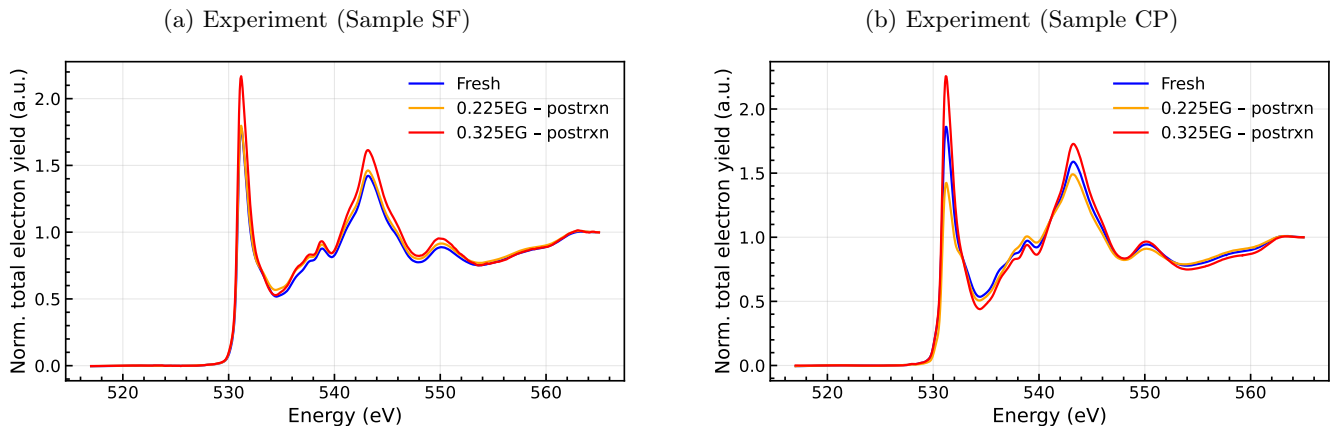


FIG. 1: O K-edge X-ray absorption spectra (XAS) of Co_3O_4 for the spray-flame synthesized sample SF (panel (a)) and the co-precipitated sample CP (panel (b)) before and after liquid-phase ethylene glycol oxidation. Each panel includes spectra for the fresh catalyst (blue), the 0.025 EG post-reaction state (orange), and the 0.325 EG post-reaction state (red). In both cases, the 0.325 EG post-reaction spectra exhibit stronger and sharper first and second peaks, indicating a more oxidized Co–O environment, consistent with the behaviour of the HT sample shown in Figure 6.

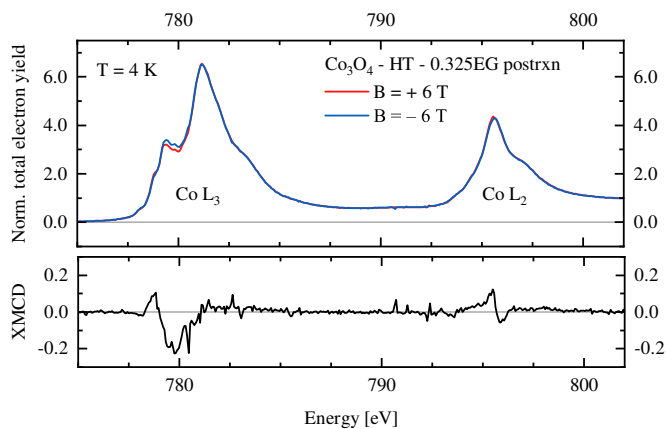


FIG. 2: Co $L_{2,3}$ -edges X-ray absorption near-edge spectra (top) and corresponding X-ray magnetic circular dichroism (bottom) of Co_3O_4 hard-templated (HT) sample after liquid-phase ethylene glycol oxidation with a concentration of 0.325 EG measured at 4 K and an applied magnetic field of 6 T.

moments of about $\pm 2.58 \mu_B$, while the following sixteen Co atoms (octahedral Co^{3+}) have moments very close to zero. This confirms the low-spin Co^{3+} configuration. Oxygen atoms exhibit only small polarization (on the order of $10^{-2} \mu_B$), and the total moment of the cell is essentially zero which is consistent with the antiferromagnetic arrangement.

Table S2 reports the same site-resolved moments for the structure containing a single oxygen vacancy. In this case, two of the octahedral Co^{3+} ions adjacent to the vacancy develop finite moments in the Co^{2+} range, indicating the local reduction of Co^{3+} to Co^{2+} induced by V_O . The rest of the Co sites keep the values they had

in the ideal structure, and only small additional polarization appears on nearby O atoms. The total magnetic moment of the supercell remains close to zero, because the two newly formed Co^{2+} moments couple antiferromagnetically.

Table S3 shows the ideal Co_3O_4 case recalculated by taking into account the spin-orbit coupling (SOC) contribution. The overall pattern is the same as in Table S1: the first eight Co^{2+} sites retain large moments, the octahedral Co^{3+} sites stay nearly nonmagnetic, and the oxygens show only minor induced polarization. SOC introduces only small quantitative changes to the individual site moments and does not modify the magnetic ordering.

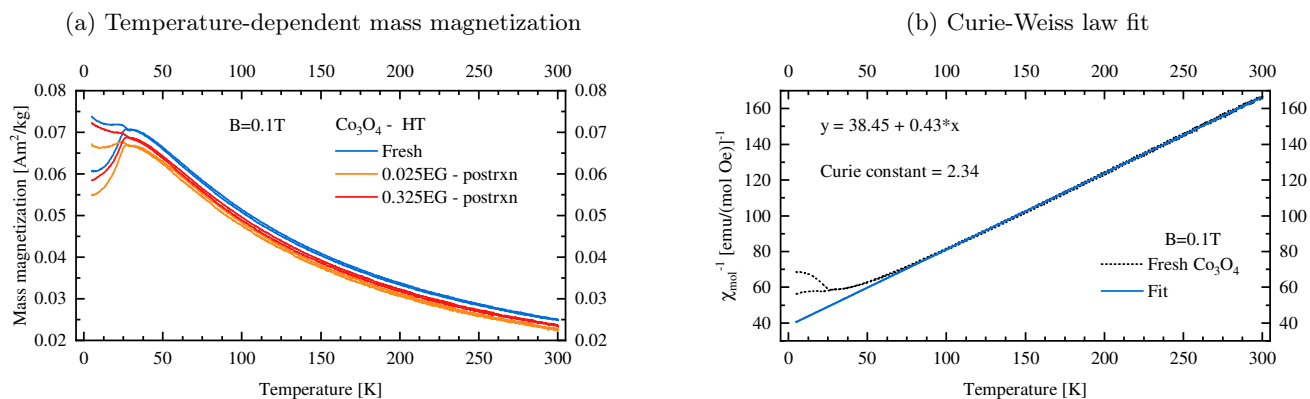


FIG. 3: (a) Temperature-dependent mass magnetization of the three hard-templated samples: fresh (blue), 0.025 EG post-reaction (orange), and 0.325 EG post-reaction (red) measured with an applied magnetic field of 0.1 T in a temperature range from 5 to 300 K. (b) Exemplary inverse molar susceptibility χ_{mol}^{-1} as a function of temperature (black dotted line) with a linear fit to obtain the Curie constant (blue) for the fresh sample.

¹ Mugiraneza, S.; Hallas, A. M. Tutorial: a beginner's guide to interpreting magnetic susceptibility data with the Curie-

Weiss law. *Communications Physics* **2022**, *5*, 95.

TABLE I: Site-resolved orbital contributions (s, p, d) and total local magnetic moments for the ideal Co_3O_4 supercell from spin-polarized DFT(+U). Ions 1–8 are tetrahedral Co^{2+} , ions 9–24 are octahedral Co^{3+} , and the remaining ions are O. Co^{2+} sites carry moments of $\sim 2.6 \mu_B$, while Co^{3+} sites are nearly nonmagnetic.

| # of ion | s | p | d | total |
|--------------|--------|--------|--------|--------|
| 1 | 0.013 | 0.050 | 2.518 | 2.581 |
| 2 | 0.013 | 0.050 | 2.518 | 2.581 |
| 3 | 0.013 | 0.050 | 2.518 | 2.581 |
| 4 | 0.013 | 0.050 | 2.518 | 2.581 |
| 5 | -0.013 | -0.050 | -2.518 | -2.581 |
| 6 | -0.013 | -0.050 | -2.518 | -2.581 |
| 7 | -0.013 | -0.050 | -2.518 | -2.581 |
| 8 | -0.013 | -0.050 | -2.518 | -2.581 |
| 9 | -0.000 | -0.000 | 0.000 | -0.000 |
| 10 | -0.000 | 0.000 | -0.000 | -0.000 |
| 11 | 0.000 | -0.000 | 0.000 | 0.000 |
| 12 | 0.000 | 0.000 | -0.000 | 0.000 |
| 13 | 0.000 | 0.000 | 0.000 | 0.000 |
| 14 | -0.000 | 0.000 | 0.000 | 0.000 |
| 15 | -0.000 | 0.000 | -0.000 | -0.000 |
| 16 | -0.000 | 0.000 | -0.000 | -0.000 |
| 17 | 0.000 | -0.000 | 0.000 | 0.000 |
| 18 | 0.000 | 0.000 | 0.000 | 0.000 |
| 19 | -0.000 | 0.000 | 0.000 | 0.000 |
| 20 | -0.000 | -0.000 | -0.000 | -0.000 |
| 21 | 0.000 | 0.000 | -0.000 | -0.000 |
| 22 | 0.000 | 0.000 | -0.000 | 0.000 |
| 23 | 0.000 | 0.000 | 0.000 | 0.000 |
| 24 | 0.000 | 0.000 | 0.000 | 0.000 |
| 25 | -0.004 | -0.029 | 0.000 | -0.033 |
| 26 | 0.004 | 0.029 | 0.000 | 0.033 |
| 27 | -0.004 | -0.029 | 0.000 | -0.033 |
| 28 | 0.004 | 0.029 | 0.000 | 0.033 |
| 29 | 0.004 | 0.029 | 0.000 | 0.033 |
| 30 | -0.004 | -0.029 | 0.000 | -0.033 |
| 31 | 0.004 | 0.029 | 0.000 | 0.033 |
| 32 | -0.004 | -0.029 | 0.000 | -0.033 |
| 33 | -0.004 | -0.029 | 0.000 | -0.033 |
| 34 | 0.004 | 0.029 | 0.000 | 0.033 |
| 35 | 0.004 | 0.029 | 0.000 | 0.033 |
| 36 | -0.004 | -0.029 | 0.000 | -0.033 |
| 37 | -0.004 | -0.029 | 0.000 | -0.033 |
| 38 | 0.004 | 0.029 | 0.000 | 0.033 |
| 39 | 0.004 | 0.029 | 0.000 | 0.033 |
| 40 | -0.004 | -0.029 | 0.000 | -0.033 |
| 41 | 0.004 | 0.029 | 0.000 | 0.033 |
| 42 | -0.004 | -0.029 | 0.000 | -0.033 |
| 43 | 0.004 | 0.029 | 0.000 | 0.033 |
| 44 | -0.004 | -0.029 | 0.000 | -0.033 |
| 45 | -0.004 | -0.029 | 0.000 | -0.033 |
| 46 | 0.004 | 0.029 | 0.000 | 0.033 |
| 47 | -0.004 | -0.029 | 0.000 | -0.033 |
| 48 | 0.004 | 0.029 | 0.000 | 0.033 |
| 49 | 0.004 | 0.029 | 0.000 | 0.033 |
| 50 | -0.004 | -0.029 | 0.000 | -0.033 |
| 51 | -0.004 | -0.029 | 0.000 | -0.033 |
| 52 | 0.004 | 0.029 | 0.000 | 0.033 |
| 53 | 0.004 | 0.029 | 0.000 | 0.033 |
| 54 | -0.004 | -0.029 | 0.000 | -0.033 |
| 55 | -0.004 | -0.029 | 0.000 | -0.033 |
| 56 | 0.004 | 0.029 | 0.000 | 0.033 |
| Total | 0.000 | -0.000 | 0.000 | -0.000 |

TABLE II: Site-resolved orbital contributions (s, p, d) and total local magnetic moments for the Co_3O_4 supercell containing a single oxygen vacancy V_{O} . Ions 1–8 are tetrahedral Co^{2+} , ions 9–24 are octahedral Co^{3+} in the ideal structure, and the remaining ions are O. Two of the octahedral Co^{3+} sites adjacent to the vacancy acquire finite moments in the Co^{2+} range, indicating local reduction induced by V_{O} .

| # of ion | s | p | d | total |
|--------------|---------------|---------------|--------------|--------------|
| 1 | 0.014 | 0.048 | 2.515 | 2.577 |
| 2 | 0.013 | 0.050 | 2.510 | 2.573 |
| 3 | 0.013 | 0.048 | 2.521 | 2.582 |
| 4 | 0.013 | 0.047 | 2.521 | 2.581 |
| 5 | -0.013 | -0.048 | -2.524 | -2.585 |
| 6 | -0.014 | -0.049 | -2.524 | -2.587 |
| 7 | -0.013 | -0.048 | -2.522 | -2.583 |
| 8 | -0.031 | -0.044 | -2.488 | -2.563 |
| 9 | 0.016 | 0.023 | 2.412 | 2.451 |
| 10 | -0.014 | -0.021 | -2.448 | -2.484 |
| 11 | 0.001 | 0.002 | 0.035 | 0.038 |
| 12 | 0.000 | 0.000 | 0.011 | 0.011 |
| 13 | -0.000 | -0.000 | -0.011 | -0.012 |
| 14 | 0.000 | 0.000 | 0.002 | 0.002 |
| 15 | 0.000 | -0.000 | -0.009 | -0.009 |
| 16 | 0.001 | 0.001 | 0.010 | 0.012 |
| 17 | -0.000 | 0.000 | 0.011 | 0.012 |
| 18 | -0.000 | -0.001 | 0.002 | 0.001 |
| 19 | 0.000 | -0.000 | 0.003 | 0.003 |
| 20 | -0.000 | -0.000 | -0.001 | -0.001 |
| 21 | 0.000 | 0.000 | 0.021 | 0.022 |
| 22 | 0.000 | -0.000 | -0.004 | -0.003 |
| 23 | -0.000 | -0.001 | -0.005 | -0.005 |
| 24 | -0.000 | 0.000 | -0.001 | -0.001 |
| 25 | -0.004 | -0.029 | 0.000 | -0.033 |
| 26 | 0.005 | 0.029 | 0.000 | 0.033 |
| 27 | -0.004 | -0.029 | 0.000 | -0.033 |
| 28 | 0.005 | 0.023 | 0.000 | 0.028 |
| 29 | 0.004 | 0.026 | 0.000 | 0.030 |
| 30 | -0.004 | -0.028 | 0.000 | -0.032 |
| 31 | 0.004 | 0.031 | 0.000 | 0.035 |
| 32 | -0.004 | -0.028 | 0.000 | -0.032 |
| 33 | -0.004 | -0.041 | 0.000 | -0.045 |
| 34 | 0.000 | -0.002 | 0.000 | -0.002 |
| 35 | 0.004 | 0.027 | 0.000 | 0.031 |
| 36 | -0.004 | -0.026 | 0.000 | -0.030 |
| 37 | -0.004 | -0.027 | 0.000 | -0.031 |
| 38 | 0.008 | 0.074 | 0.000 | 0.082 |
| 39 | 0.004 | 0.024 | 0.000 | 0.028 |
| 40 | -0.003 | -0.041 | 0.000 | -0.044 |
| 41 | 0.008 | 0.072 | 0.000 | 0.080 |
| 42 | -0.005 | -0.043 | 0.000 | -0.048 |
| 43 | 0.001 | -0.011 | 0.000 | -0.010 |
| 44 | -0.003 | -0.039 | 0.000 | -0.042 |
| 45 | 0.000 | 0.001 | 0.000 | 0.001 |
| 46 | -0.004 | -0.029 | 0.000 | -0.033 |
| 47 | 0.008 | 0.073 | 0.000 | 0.081 |
| 48 | 0.004 | 0.021 | 0.000 | 0.025 |
| 49 | -0.009 | -0.056 | 0.000 | -0.065 |
| 50 | -0.004 | -0.027 | 0.000 | -0.031 |
| 51 | 0.004 | 0.025 | 0.000 | 0.029 |
| 52 | 0.004 | 0.025 | 0.000 | 0.029 |
| 53 | 0.000 | -0.017 | 0.000 | -0.017 |
| 54 | -0.004 | -0.028 | 0.000 | -0.032 |
| 55 | 0.004 | 0.023 | 0.000 | 0.027 |
| Total | -0.007 | -0.021 | 0.038 | 0.010 |

TABLE III: Site-resolved orbital contributions (s, p, d) and total local magnetic moments for the ideal Co_3O_4 supercell recalculated with spin-orbit coupling (SOC) in the z direction. Ions 1–8 are tetrahedral Co^{2+} , ions 9–24 are octahedral Co^{3+} , and the remaining ions are O. SOC causes only minor quantitative changes and preserves the overall magnetic pattern of the ideal spinel.

| # of ion | s | p | d | total |
|--------------|--------|--------|--------|--------|
| 1 | 0.013 | 0.050 | 2.515 | 2.579 |
| 2 | 0.013 | 0.050 | 2.515 | 2.579 |
| 3 | 0.013 | 0.050 | 2.515 | 2.579 |
| 4 | 0.013 | 0.050 | 2.515 | 2.579 |
| 5 | -0.013 | -0.050 | -2.515 | -2.579 |
| 6 | -0.013 | -0.050 | -2.515 | -2.579 |
| 7 | -0.013 | -0.050 | -2.515 | -2.579 |
| 8 | -0.013 | -0.050 | -2.515 | -2.579 |
| 9 | -0.000 | 0.000 | 0.000 | 0.000 |
| 10 | -0.000 | 0.000 | 0.000 | 0.000 |
| 11 | -0.000 | -0.000 | -0.000 | -0.000 |
| 12 | 0.000 | 0.000 | 0.000 | 0.000 |
| 13 | -0.000 | 0.000 | 0.000 | 0.000 |
| 14 | 0.000 | 0.000 | 0.000 | 0.000 |
| 15 | 0.000 | 0.000 | 0.000 | 0.000 |
| 16 | 0.000 | -0.000 | -0.000 | -0.000 |
| 17 | -0.000 | -0.000 | -0.000 | -0.000 |
| 18 | -0.000 | 0.000 | 0.000 | 0.000 |
| 19 | -0.000 | 0.000 | 0.000 | 0.000 |
| 20 | 0.000 | -0.000 | -0.000 | -0.000 |
| 21 | -0.000 | 0.000 | 0.000 | 0.000 |
| 22 | 0.000 | 0.000 | 0.000 | 0.000 |
| 23 | 0.000 | 0.000 | 0.000 | 0.000 |
| 24 | -0.000 | 0.000 | 0.000 | 0.000 |
| 25 | -0.004 | -0.029 | 0.000 | -0.033 |
| 26 | 0.004 | 0.029 | 0.000 | 0.033 |
| 27 | -0.004 | -0.029 | 0.000 | -0.033 |
| 28 | 0.004 | 0.029 | 0.000 | 0.033 |
| 29 | 0.004 | 0.029 | 0.000 | 0.033 |
| 30 | -0.004 | -0.029 | 0.000 | -0.033 |
| 31 | 0.004 | 0.029 | 0.000 | 0.033 |
| 32 | -0.004 | -0.029 | 0.000 | -0.033 |
| 33 | -0.004 | -0.029 | 0.000 | -0.033 |
| 34 | 0.004 | 0.029 | 0.000 | 0.033 |
| 35 | 0.004 | 0.029 | 0.000 | 0.033 |
| 36 | -0.004 | -0.029 | 0.000 | -0.033 |
| 37 | -0.004 | -0.029 | 0.000 | -0.033 |
| 38 | 0.004 | 0.029 | 0.000 | 0.033 |
| 39 | 0.004 | 0.029 | 0.000 | 0.033 |
| 40 | -0.004 | -0.029 | 0.000 | -0.033 |
| 41 | 0.004 | 0.029 | 0.000 | 0.033 |
| 42 | -0.004 | -0.029 | 0.000 | -0.033 |
| 43 | 0.004 | 0.029 | 0.000 | 0.033 |
| 44 | -0.004 | -0.029 | 0.000 | -0.033 |
| 45 | -0.004 | -0.029 | 0.000 | -0.033 |
| 46 | 0.004 | 0.029 | 0.000 | 0.033 |
| 47 | -0.004 | -0.029 | 0.000 | -0.033 |
| 48 | 0.004 | 0.029 | 0.000 | 0.033 |
| 49 | 0.004 | 0.029 | 0.000 | 0.033 |
| 50 | -0.004 | -0.029 | 0.000 | -0.033 |
| 51 | -0.004 | -0.029 | 0.000 | -0.033 |
| 52 | 0.004 | 0.029 | 0.000 | 0.033 |
| 53 | 0.004 | 0.029 | 0.000 | 0.033 |
| 54 | -0.004 | -0.029 | 0.000 | -0.033 |
| 55 | -0.004 | -0.029 | 0.000 | -0.033 |
| 56 | 0.004 | 0.029 | 0.000 | 0.033 |
| Total | -0.000 | -0.001 | 0.001 | 0.001 |